Polarized Optical Absorption Spectroscopy, NEXAFS, and GIXRD Measurements of Chain Alignment in Polyfluorene Thin Films

H. Cheun,[†] X. Liu,[‡] F. J. Himpsel,*,[‡] M. Knaapila,[§] U. Scherf,[||] M. Torkkeli,[⊥] and M. J. Winokur*,[‡]

Department of Materials Science and Department of Physics, University of Wisconsin, Madison, Wisconsin 53706; MAX-lab, Lund University, SE-22100 Lund, Sweden; Makromolekulare Chemie, Bergische Universität, D-42097, Wuppertal, Germany; and Department of Physics, University of Helsinki, Fl-00014 Helsinki, Finland

Received November 20, 2007; Revised Manuscript Received June 17, 2008

ABSTRACT: The uniaxial chain alignment of low molecular weight poly(9,9-bis(ethylhexyl)fluorene-2,7-diyl) (PF2/6) in thin films cast atop rubbed polyimide templates is characterized by polarized optical absorption spectroscopy, carbon K near-edge X-ray absorption fine structure spectroscopy (NEXAFS), and grazing incidence X-ray diffraction (GIXRD) in response to thermal annealing and increasing film thickness (ca. 15–150 nm). The highest overall levels of uniaxial alignment are obtained in the thinnest PF2/6 films. However, the orientation of chains at the top surface after thermal annealing is nearly thickness independent despite a large drop in the maximum optical dichroic ratio as the film thickness increases. The kinetics of chain alignment on heating are strongly film thickness dependent and only weakly correlated with a crossover to a nematic liquid crystal state. All told these data support a structural model in which there is a graded morphology such that the top and bottom surfaces exhibit appreciable planar, uniaxial alignment while the film interior includes a greater proportion of nonplanar (i.e., tilted) chains after thermal cycling. These inhomogeneities are likely to influence technologically important optical and transport properties.

Introduction

Conjugated polymers (CPs) continue to receive worldwide attention as an attractive companion device technology to more conventional semiconductors because of the unique ability to broadly tune CP properties through direct chemical synthesis and then utilize facile, low-cost processing procedures.[1–4] Central to many CPs device applications is an overt reliance on the fabrication of polymer thin films. These films often include distinctive attributes spanning multiple length scales, and variations in the structure can strongly affect both the optical and electronic properties. There are important questions relating to the molecular level chain conformations,[5] the intermolecular self-organization,[6] and overall chain alignment[7] in the film interior as well as at surface interfaces.[8,9] Understanding and controlling these structures is an essential step for optimizing existing device performance or obtaining new functionality.

Especially interesting is the ability to achieve planar uniaxial chain orientation in thin films. In this arrangement the chains lie parallel to surface (homogeneous alignment), and their axes point, on average, along a single direction. This alignment of CP chains can dramatically enhance charge transport in field-effect transistor devices[7] or lead to highly polarized optical emission in light-emitting diodes.[10] Many methods are available for producing uniaxial alignment, and examples of these include stretch orientation,[11] friction transfer,[12,13] direct surface rubbing,[14] directional crystallization,[15] and surface-induced alignment.[16–18] Alignment at a templating interface is a particularly promising method for producing high levels of anisotropy. Rubbed polyimide (PI) substrates[19] are commonly used, but good alternatives do exist [e.g., poly(*N*-vinylcarbazole)[20] or azobenzene derivatives[21–23]]. Typically, a thermotropic liquid crystalline CP is spin-cast atop the substrate, and then the film is annealed at temperatures above which the CP transforms into a nematic mesophase or isotropic melt. Banach et al.[24] investigated the influence of molecular weight (MW) on thermotropically aligned fluorene–benzothiadiazole copolymers and observed that lower MW materials flowed more easily and yielded higher dichroic ratios. Higher MWs[25] are typically associated with better transport properties, and so, as is often the case in these polymers, there can be conflicting traits.

Among CPs, polyfluorenes (PFs) are widely studied as technologically important blue-emitters with excellent chemical stability, high photoluminescent quantum yields, and good transport characteristics.[5,26] Many functionalized PFs are characterized by a so-called hairy-rod-type structure and are amenable to large-scale chain alignment. Alignment of PF on rubbed PI substrates was initially demonstrated by Grell et al.,[10] and many factors affect this process. A prototypical branched PF, poly(9,9-bis(ethylhexyl)fluorene-2,7-diyl) or PF2/6, has been extensively studied by Knaapila et al.[27–29] In PF2/6 the observed dichroic ratios are again strongly sensitive to MW. PF2/6 is especially notable because of the appearance of near-5-fold helices[30–32] and a MW-dependent transition between a nematic liquid crystal (*n*-LC) state and a hexagonal (hex) crystalline phase, the latter of which yields a full three-dimensional (3D) textured orientation of the unit cell in cast films formed on templating substrates.[29]

Recently, there have been a number of notable studies characterizing the extent of chain orientation at the film surface by near-edge X-ray absorption fine structure spectroscopy (NEXAFS).[14,33–35] A key finding is that uniaxial alignment propagates many tens of nanometers away from the templating interface to give substantial chain orientation at the top surface. Pattison et al.[34] observed high levels of planar–uniaxial alignment in polyfluorene–thiophene copolymers parallel to the rubbing direction. Analogous results are found in a study of functionalized polythiophene thin films by Delongchamp, Gurau,

---

* Corresponding authors. E-mail: mwinokur@wisc.edu or fhimpsel@facstaff.wisc.edu.

[†] Department of Materials Science, University of Wisconsin.

[‡] Department of Physics, University of Wisconsin.

[§] Lund University.

[||] Bergische Universität.

[⊥] University of Helsinki.

10.1021/ma702579r CCC: $40.75

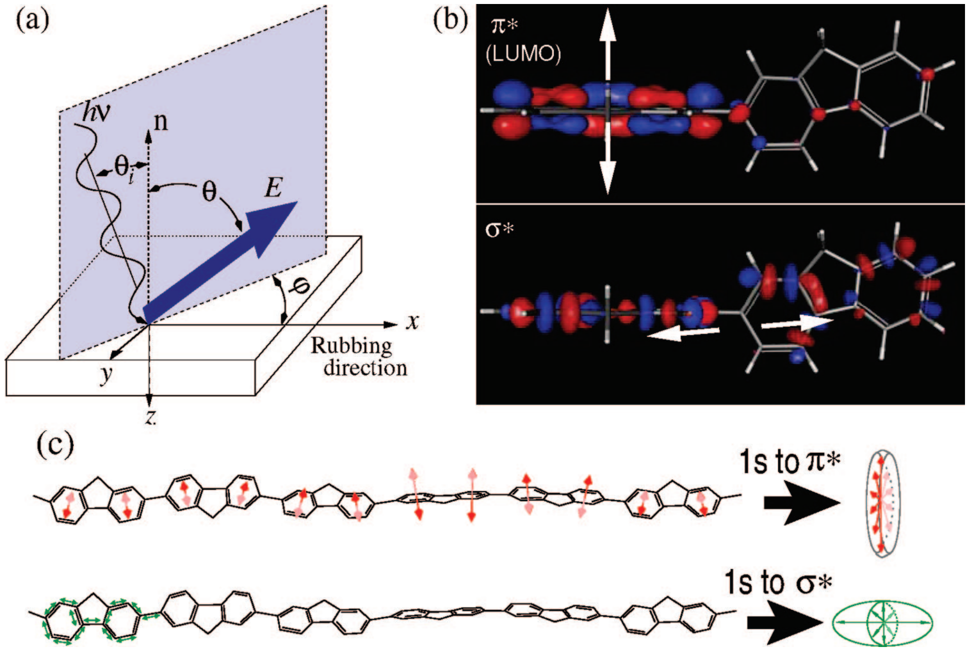

Figure 1. (a) NEXAFS geometry with $\theta \equiv$ polar angle, $\varphi \equiv$ azimuthal angle, and $E =$ electric field vector of the incident light in conjunction with the rubbing direction of the polyimide substrate. (b) Example π^* (top) and σ^* orbital wave function isosurfaces from an ab initio calculation using a fluorene dimer and a STO-3G basis set. In this example the phenylene planes of the two fluorenes are nearly orthogonal. The white arrows show the direction of the transition dipole moments associated with the NEXAFS C_{1s} to π^* and σ^* transitions. (c) Carbon skeletal backbone of the PF2/6 nominal 5/2 helix showing the cylindrical averaging of the C_{1s} to π^* (top) and σ^* (bottom) transitions.

and co-workers,[36,37] and in their work, the effect of thermal processing is documented. Alternatively, the carbon K edge of aligned PF2/6 fibers has been probed by nonresonant inelastic X-ray scattering.[38] Despite this progress, there have been few direct observations of the explicit temperature-dependent behavior of these films as chain alignment ensues or, as far as we are aware of, PF2/6 studies that assess surface alignment as a function of increasing film thickness.[39]

This paper reports experimental observations of the chain alignment process in low-molecular-weight PF2/6 thin films cast onto rubbed PI substrates. Here we have employed in situ monitoring of the polarized UV−vis absorption to document and maximize the extent of chain alignment and then ex situ, carbon K-edge NEXAFS spectroscopy to assess the extent of chain alignment at the top surface in films of differing thickness. In situ grazing-incidence X-ray diffraction (GIXRD) provides a complementary measure of chain alignment and structural order. These results show that temperature, time, and film thickness all influence the uniaxial orientation of the PF2/6 chains. The NEXAFS data indicate that the extent of chain alignment at the top surface is retained in films at least as thick as 60 nm. Taken together, these results indicate the existence of graded morphologies[40] in which extensive homogeneous uniaxial alignment occurs at both the top and bottom surfaces, but the film interior itself includes less planar alignment.

Experimental Section

Low-molecular-weight poly(9,9-bis(ethylhexyl)fluorene-2,7-diyl) ($M_n = 13$, $M_w = 23$, in kg/mol, 13/23-PF2/6) was synthesized using previously reported methods. At this MW PF2/6 initially adopts a nematic glassy state and undergoes a thermotropic transition to a *n*-LC mesophase at temperatures just below 100 °C. Four different solutions, at 5, 10, 20, and 50 mg/mL of 13/23-PF2/6, were prepared using spectroscopic grade toluene as a solvent. Fifty microliters of each solution was deposited onto commercial glass/indium−tin oxide (ITO)/rubbed PI substrates (EHC Co. Ltd., Japan) and then spin-cast at 2500 rpm for 60 s with the more dilute solutions giving the thinnest films. The PI, ITO, and glass thicknesses are approximately 30 nm, 100 nm, and 1 mm, respectively. The ITO coating is especially useful for alleviating the most severe effects of charging during the NEXAFS measurements. The nominal film thicknesses from these four solution concentrations are 15, 30, 60, and 150 nm, respectively. Afterward, these films were transferred into a vacuum-insulated oven/cryostat and then characterized in situ using a custom-built dual photoabsorption/photoluminescence (AB/PL) spectrometer. A focused 200 μm diameter spot was used for AB measurements. A Glan-Thomson polarizer was inserted into the optical path of the incident white light beam, and spectra were taken with the polarizer orientated parallel and perpendicular to the rubbing direction of the PI substrate. The layout is schematically shown in Figure 2c. Thermotropic alignment was achieved by a continuous warming of these films up to a temperature of 220 °C. After thermal treatment the films were rapidly cooled to room temperature (RT).

All dichroic ratios ($\mathrm{DR} = \mathrm{AB}_{\|}/\mathrm{AB}_{\perp}$) were assessed at the nominal maximum absorption in the AB profile (ca. 3.25 eV). Rotating the UV polarizer about its optical axis induced slight lateral displacements of the focal spot, and so it was necessary to translate the polarizer in order to maintain the focus at a fixed position on the substrates. The dichroic ratios also reflect the extent of uniaxial order, and this can be restated in terms of an order parameter

$$S \geq [\mathrm{DR} - 1]/[\mathrm{DR} + (d - 1)]$$

where d reflects the dimensionality of systems. S is defined to be along the PI rubbing direction (i.e., the x axis direction), and here we assume the transition dipole is perfectly parallel to the chain axis.[10,41] In the case of fully planar chain alignment then there are no chains tilted toward the surface normal (i.e., the z axis direction), and $d = 2$ [for S_{2D}] should be used. If the chain axes are nonplanar (i.e., a homeotropic component) and one assumes cylindrical symmetry about the chain axes, then $d = 3$ [for S_{3D}] is a representative limiting case. In the thinnest PF2/6 films planar alignment dominates, and thus S_{2D} is appropriate. Nonplanar alignment may occur in thicker films, and in this case, S_{3D} may be more appropriate. A rough sketch of the PF film morphology and a typical AFM image of the surface are shown in Figure 2.

By employing polarized light incident at oblique angles (here 45°), one can employ s- or p-polarized incident light, and this allows

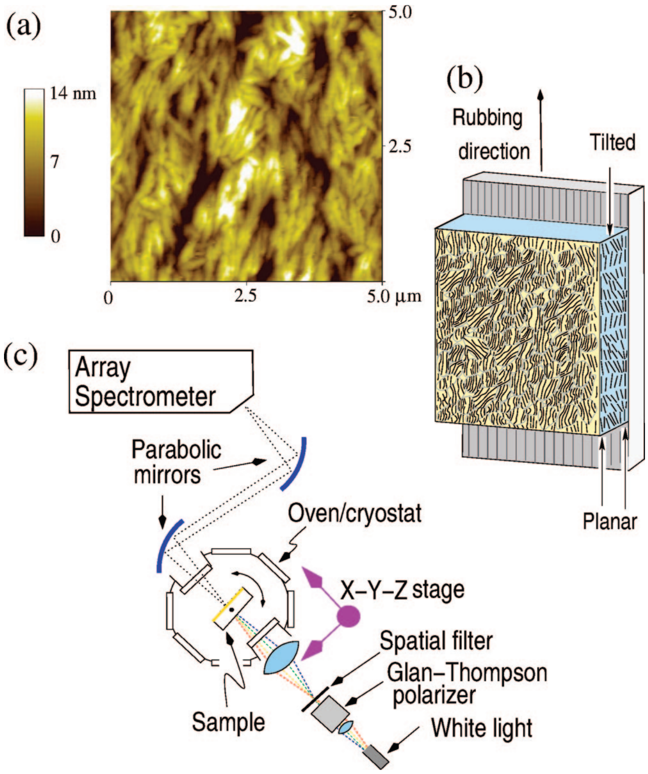

Figure 2. (a) Tapping-mode atomic force microscopy height image of a low-MW PF2/6 film (ca. 60 nm thick, UV−vis DR 8) cast atop rubbed polyimide after thermal annealing. (b) Schematic of the PF2/6 film on a rubbed polyimide substrate showing partial homogeneous, uniaxial alignment. The homeotropic tilting of the polymer chains increases in the film interior. (c) Schematic of the scanning UV−vis absorption set up along horizontal. The PF2/6 thin film samples are mounted with the substrate rubbing direction along the vertical (i.e., out of the plane of the paper).

for probing chains having nonplanar alignment (e.g., a component perpendicular to the film surface). In this case the fraction of chains pointing along the x, y, and z can be specified as N_x, N_y, and N_z, respectively, to give complex refractive indices $n_i = n_0 + N_i(\Delta n + \Delta k)$, where n_0 is the PF2/6 value perpendicular to the chain axis and Δn and Δk are the respective differences between the real and imaginary refractive indices parallel and perpendicular to the chain axis. Here we use values reported by Lyon and Monkman.[9] Because of the PI rubbing direction, one must define s- and p-type polarizations in terms of components parallel and perpendicular to the rubbing direction and obtain two distinct values of AB_s and AB_p. Analysis of Maxwell's equations in this situation [going from vacuum (i) into a thin-film medium (t)] leads to the complex form of Snell's law, $\sin \theta_i = \hat{n}_t \sin \theta_t$, where both $\hat{n}_t$ and θ_t are complex. In general, $\cos \theta_t = a + ib/\hat{n}_t$, but for the case of oblique incidence and s-type polarization (TE mode), the absorption coefficient along the z axis, $\alpha(\theta_i)$, is proportional to the product bz, where b is the coefficient perpendicular to the surface normal with $b^2 = [(n^2 - k^2 - \sin^2 \theta_i) + 4n^2k^2]^{1/2} - (n^2 - k^2 - \sin^2 \theta_i)$. Different values of b occur with the $\vec{E}$-field parallel to the x and y axes (i.e., b_x and b_y with corresponding n_x, n_y, k_x, and k_y). A similar result is obtained in the case of p-type polarization. This explicit formalism and the associated transmission coefficients are comprehensively described in papers by Mosteller and Wooten[42] or Wang.[43] Characterization by this method was only pursued in the case of the 150 nm thick film (spin-cast from the 5% solution) because of the very large AB values in both the parallel and perpendicular directions.

NEXAFS spectroscopy was performed at the C K-edge with total electron yield (TEY) detection using both the Synchrotron Radiation Center (SRC) of the University of Wisconsin−Madison and the Advanced Light Source (ALS) at Berkeley. Two different sets of samples were studied at the respective light sources, and these correspond to "series I" (only at SRC) and "series II" (only at the ALS). For series I six samples were prepared, and then three were thermally annealed while monitoring the UV−vis absorption. In series II only three postannealed samples were used. The polarization, P, at both beamlines was 0.9 [with $P \equiv I_{\|}/(I_{\|} + I_{\perp})$]. TEY probes the surface to a depth of 2−10 nm[44−47] by collecting Auger electrons from both the core hole and the secondary electrons created by them. All spectra were normalized to the photocurrent from an upstream Au grid which was acquired simultaneously. The photon energy was calibrated to the π^* peak of graphite at 285.4 eV to give an absolute accuracy of 0.2 eV. Homogeneity of the samples was confirmed by collecting two or three spectra at different locations for each sample. In addition, several consecutive scans were performed at the same location to assess the extent of radiation damage to the samples under soft X-ray illumination. No appreciable radiation damage was detected after three consecutive scans. This was consistent with the photon flux density, which was low enough to keep the number of absorbed photons small compared to the number of molecules in the exposed spot. Some effects of charging could be seen in all samples. The impact was most severe in the series II data because of the higher incident flux at the ALS.

To investigate the backbone orientation of the polymer film surface, polarization-dependent NEXAFS spectra were collected by varying the angle of incidence using p-polarized light. As shown in Figure 1a, the polar angle θ is defined as the angle between the electric field vector of the synchrotron light and the sample normal. The azimuthal angle φ is defined as the angle between the plane of incidence and the rubbing direction. At φ equal to 0° and 90°, the spectra were collected at various polar angles. A linear background was subtracted from these spectra by fitting to the pre-edge energy region. This accounts for absorption from valence states. The resulting spectra were also normalized to a common step height between the pre- and post-absorption edge regions, which makes them directly proportional to the absorption per carbon atom.

The dipole selection rules for transitions from the 1s core levels allow final states with p-character. The NEXAFS intensity follows a $\cos 2\delta$ distribution, where δ is the angle between the electric field vector of the incident light and the soft X-ray transition dipole. For an individual isolated fluorene monomer the transition dipole is perpendicular to the plane defined by the two fused phenylene rings. A simple ab initio quantum chemical calculation[48] of a fluorene dimer (with nearly orthogonal orientation of the two monomers) yields a π^* (LUMO) wave function with isocontours above and below the plane formed by the left-hand-side phenylene ring (see Figure 1b) and a transition dipole normal to this phenylene ring plane. Because of the forced near orthogonality of this example dimer, the LUMO electron wave function is mostly isolated onto a single monomer. In PF2/6 the LUMO and wave functions at slightly higher energies correspond to the TEY NEXAFS peak near 285.4 eV. At somewhat higher energies there are eigenfunctions exhibiting more s-like character and have wave function isocontours along the C−C bonds (see Figure 1b again). These are associated with a carbon 1s to σ^* transition and form a peak near 292 eV. Here the transition dipole moment (TDM) is oriented more along the long axis of the molecule.

In PF2/6 the nominal 5/2 helical structure along the backbone produces a near-cylindrical averaging of the π-orbital direction (see Figure 1c) about a ring perpendicular to the chain axis. When the E-field is parallel to the chain axis, it is nearly perpendicular to all of these transition dipoles, and thus the soft X-rays have a larger optical depth. Very few electrons are produced in the 1−2 nm layer of the film surface, and thus the observed NEXAFS intensity of the 285.4 eV peak is at a minimum. In contrast, the 1s−2σ^* transition peak, centered near 293 eV, is sensitive to the orientation of fluorene backbone σ-bonds. In this case there are transition dipole components both parallel and perpendicular to the chain axis (in a nominal ratio of 2 to 1), and so this peak is typically strongest when the 1s−π^* feature is weakest.

Plotting the integrated intensity of the 1s−π* peaks (rescaled to the maximum intensity at $\theta = 30°$) with respect to $\sin^2 \theta$ typically gives a straight line, and finding the slope and intercepts (see refs 34 or 49 for details) yields three orientation factors f_x, f_y, f_z of the TDM subject to the constraint $f_x + f_y + f_z = 1$. These can be related to an order parameter parallel to a specified axis. In ref 50, the expression $^1/_2(3f_z - 1)$ is used, and this become unity if all the TDMs point along the *z*-axis. The situation is different for PF2/6. In the limiting case that all chains are perfectly aligned parallel to the *x*-axis (the rubbing direction) then, because of the helical chain structure, then all the TDMs lie nearly normal to the *x*-axis and $f_z = f_y \gg f_x$. In this case we employ an order parameter $S = 2\,[^1/_2(3f_z - 1) + {^1/_2}(3f_y - 1)] = 1 - 3f_x$, and this describes the extent of surface chain alignment parallel to the rubbing direction. If all TDMs were perfectly perpendicular to the PF chain axis and all chains perfectly parallel to the *x*-axis, then $f_z = f_y = 0.50$ and $S = 1$. Alternatively, if all the chains were isotropically arranged, then $f_x = f_y = f_z = 1/3$ and $S = 0$. The special cases of homogeneous and cylindrically uniform homeotropic alignment have respectively $S = 0.25$ with $f_x = f_y = 0.25, f_z = 0.50$ and $S = -0.50$ with $f_x = f_y = 0.50, f_z = 0.0$. Head-to-head comparisons between the UV−vis dichroic ratio and this order parameter are not possible (they measure different things). However, one can use the limiting case (i.e., all 1s−π* TDMs are perpendicular to the chain axis) to estimate of the fractional number of chain segments, N_x, N_x, and N_z, oriented along a particular axis by using the three permutations of the expression $2f_i = N_j + N_k$ where *i*, *j*, and *k* reflect the three axes. It should be noted that the uncertainty associated with a particular f_i ($i = x$, y, or z) typically ranged from 0.003 to 0.016, and thus the uncertainty of a given *N* could reach 0.03.

Alternatively, one can arbitrarily assume complete homogeneous alignment ($N_z \equiv 0$) and then determine N_x and N_y (with $N_x + N_y = 1$) by introducing the assumption that the inherent PF2/6 TDM parallel to the chain axis, f_c, is small but finite. The carbon 1s to π* TDM is largely perpendicular to the chain axis. We expect that the actual situation is likely intermediate to these two limiting cases, and the derived N_z values, under the assumption that all the TDMs are perpendicular to the polymer chain axis, represent an upper limit on the out of plane chain orientation at the film surface.

Once values of N_x and N_y are obtained then the ratio N_x/N_y is equivalent to the DR from the polarized absorption studies. Thereafter, comparable order parameters S_{2D} and S_{3D} can be obtained using the N_x/N_y ratios for the NEXAFS results under the assumption that $f_c \equiv 0$ and then $N_z \equiv 0$.

GIXRD measurements were performed at the W1.1 (ROEWI) beamline at HASYLAB in Hamburg, Germany. The beam, 10.5 keV, 0.07 × 0.4 mm (vertical × horizontal), was monochromatized using a double Si(111) crystal and focused onto the sample. Additional antiscatter slits placed close to the sample and a helium atmosphere were used to reduce the background and limit radiation damage. To maximize the signal from the thin PF2/6 layer, experiments were conducted at a grazing angle close to the critical angle of the PF2/6 layer ($\theta = 0.12°$ at 10.5 keV). The scattering patterns were recorded using an image plate (Molecular Dynamics) detector with the X-ray beam either parallel or perpendicular to the substrate PI rubbing direction (i.e., the *x*-axis). The parallel configuration (incident beam nearly parallel to the *x*-axis) gives an Ewald projected pattern approximating the equatorial in-plane scattering [(*hk*0) or, in regard to Figure 1, (*zy*0)] while the latter, along the *y*-axis, gives both meridional out-of plane scattering and equatorial scattering [i.e., from (*h*0*l*) to (0*kl*) or (*z*0*x*)]. These data were normalized to the incident flux using an ionization chamber mounted just before the sample. The instrumental resolution function was found to be negligible. The temperature scans were performed in situ using a LakeShore 330 Autotuning temperature controller.

Results and Discussion

Polarized Photoabsorption. As a prelude to the subsequent NEXAFS studies, the overall process of chain alignment was monitored in situ using polarized AB. In this study only a single polarization could be tracked. This was chosen to be perpendicular to the rubbing direction because of the very large reductions in the $AB_\perp$ during thermal annealing. Increasing uniaxial alignment is associated with a monotonic reduction in the optical density in the perpendicular direction. Increased alignment parallel to the PI rubbing direction or perpendicular to the film surface (i.e., nonplanar alignment) may be correlated with this drop in the optical density. Planar alignment of PF2/6 chains at surface interfaces has been well documented, but the chain orientation in the film interior is less known. We also note that thermal annealing derived reductions in the average optical density may relate to changes in the chain alignment or evolution in the nematic domain structure.[51]

Figures 3a−c document the polarized ABs (at normal beam incidence) of three increasingly thick PF2/6 films at room temperature (rt) immediately before and after annealing. These samples reflect nominal thicknesses of 15, 30, and 60 nm using the respective PF2/6−toluene solutions of 5, 10, and 20 mg/mL. Weak AB anisotropy is initially present in all three as-cast films with the thinnest films generally exhibiting the largest anisotropy. Explicit values of the DR and *S* are shown in the first three columns of Table 1.

Thermal annealing produces large increases in the optical anisotropy with significantly larger DRs in the thinner films (again see Table 1). In general, the magnitude of the drop in the $AB_\perp$ exceeds the gain in the $AB_\parallel$, and this attribute may be associated with the growth and reorientation of the nematic domains.[51] The maximum DR recorded is just over 40, but it is difficult to be exact because of the small optical density in the perpendicular direction and slight systematic drifts in the reference spectra. There is also a distinctive change in the line shape of the perpendicular AB with a shift in the peak absorption to higher photon energy. After thermal annealing the parallel absorption has a more pronounced leading edge and its maximum at 3.18 eV, whereas the perpendicular absorption peak has a more gradual rise and a maximum near 3.5 eV. The latter blue shift is ostensibly associated with more conformationally disordered regions of the film (e.g., amorphous fractions). Preferential alignment of nematic domains as opposed to more amorphous regions of the film is a commonly forwarded explanation.

In general, thicker PF2/6 films exhibit the most noticeable red shift in the $AB_\parallel$ profile in response to thermal annealing. This trend is further documented in a follow-up study of an even thicker film (see Figure 4a) which only achieved a modest final DR of 6.3. Here the leading edge of the AB profile parallel to the chain axis becomes even more sharply defined after annealing. We also note that variations in the molecular level order or in the distribution of nematic domains at larger length scales can both potentially influence the observed line shape. In this instance the film was examined with a polarized beam having an oblique (i.e., 45°) angle of incidence. Figures 4b,c exhibit the AB for s- and p-type polarizations with the plane-of-incidence (POI) first parallel and then perpendicular to the rubbing direction (along the *x*-axis). In the case of $AB_{s\perp}$ (POI⊥*x*) the *E*-field of the incident beam is parallel to the *x*-axis, and this should give an absorption profile that is roughly comparable to that seen with normal incidence. On the other hand, the $AB_{p\parallel}$ (POI‖*x*) data has a component *E*-field normal to the surface, and if there are only planar aligned chains, then this *E*-field component will not be strongly attenuated. Thus, the measured maximum in absorption maximum should be noticeably reduced. In Figure 4b the $AB_{p\parallel}$ curve is only slightly less than the $AB_{s\perp}$ curve in Figure 4c, and so there is evidence of appreciable PF2/6 tilting away from planar alignment in this film. We also observe that the $AB_{p\parallel}$ is noticeably weaker than the $AB_{s\perp}$.

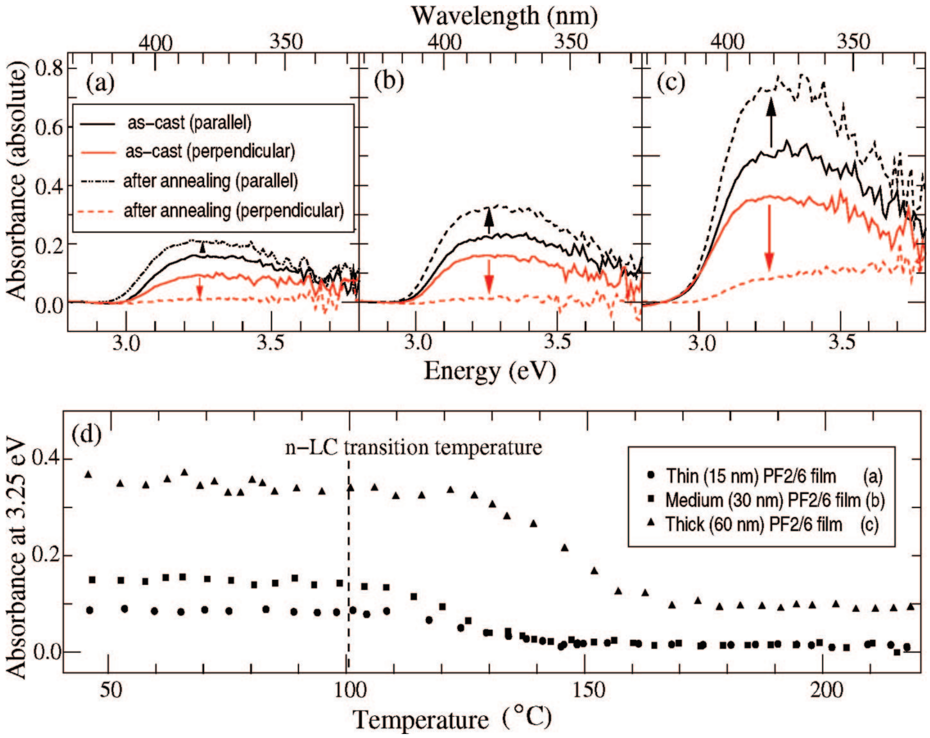

Figure 3. Top: polarized UV−vis absorption spectra of three increasingly thick PF2/6 films, "thin" or 15 nm (a), "medium" or 30 nm (b), and "thick" or 60 nm (c) from series I (see Table 1) before and after thermal annealing. Bottom: (d) temperature dependence of the UV−vis absorption at 3.25 eV perpendicular to the rubbing direction of the three samples (a−c) recorded in situ.

Table 1. Comparison of the 2D and 3D Orientational Order Parameters from Polarized UV−vis Absorption and NEXAFS Data[a]

	UV−vis			NEXAFS ($f_c \equiv 0$)				NEXAFS ($N_z \equiv 0$)			
film	DR	S_{2D}	S_{3D}	N_x	N_y	N_z	S_{3D}	N_x	N_y	f_c	S_{2D}
series I											
as-cast, (15 nm)	1.9	0.32	0.24	0.51	0.29	0.19	0.20	0.74	0.26	0.09	0.48
annealed	41	0.95	0.93	0.76	0.15	0.08	0.6	0.90	0.10	0.04	0.8
as-cast (30 nm)	1.4	0.17	0.12	0.48	0.43	0.09	0.04	0.53	0.47	0.04	0.06
annealed	40	0.95	0.93	0.76	0.14	0.10	0.6	0.93	0.07	0.05	0.9
as-cast (60 nm)	1.4	0.17	0.12	0.45	0.44	0.11	0.00	0.50	0.50	0.06	0.01
annealed	8.9	0.80	0.72	0.76	0.13	0.10	0.6	0.94	0.06	0.05	0.9
series II											
as-cast (15 nm)	1.3	0.12	0.08								
annealed	19	0.90	0.86	0.82	0.14	0.02	–	1.15	−0.15	0.08	–
as-cast (30 nm)	1.9	0.31	0.08								
annealed	23	0.92	0.88	0.81	0.01	0.16	–	1.30	−0.30	0.01	–
as-cast (60 nm)	1.5	0.20	0.15								
annealed	8.4	0.79	0.71	0.83	0.08	0.08	–	0.98	0.02	0.04	–
150 nm thick film											
as-cast	1.1	0.05	0.03								
annealed	6.3	0.72	0.63								

[a] The respective NEXAFS values are obtained under the assumption that the 1s to π^* TDM is perfectly perpendicular to the polymer chain axis ($f_c \equiv 0$ for 3D) or that the PF2/6 chains have completely homogeneous alignment ($N_z \equiv 0$ for 2D; see the Experimental Section for further discussion).

In Table 2 the observed ratios of $AB_{s\perp}/AB_{p\parallel}$ and $AB_{s\parallel}/AB_{p\perp}$ (at 3.25 eV) are compared to those calculated assuming various nominal values of N_x, N_y, and N_z and the appropriate expression for b having s- or p-type polarizations with the POI parallel and perpendicular to the x-axis. The third case, in which N_z is 0.26, is qualitatively most consistent with the experimental data. Ideally, this calculation should reflect the nematic domain morphology and the possibility that the morphology varies from the surface into the film interior.

Figure 3d depicts the perpendicular polarized AB at 3.25 eV of three different films during thermal annealing. These data give some insight into the kinetics of the alignment process. For this specific PF2/6 MW the thermotropic *n*-LC phase transition occurs just under 100 °C according to the phase diagram of Knaapila et al.[29] Temperatures near 100 °C produce *no* appreciable change in the perpendicular AB. The onset of the anticipated drop in the perpendicular absorption (indicating an increase in uniaxial alignment) of the two thinner films begins at 115 °C and is completed at approximately 145 °C. In the thicker film the onset of chain alignment occurs at a temperature closer to 125 °C and is completed at 160 °C. Slower, stepwise heating of other samples (and at higher MWs, not shown) yields comparable results. Moreover, extended annealing at elevated temperatures produces little improvement in the DRs. The majority of the chain alignment occurs relatively rapidly once a threshold temperature some 15−30 °C above that of the nominal transition temperature to the *n*-LC state. These results suggest that other factors, such as pinning of the chains at the polyimide interface or by chain entanglement, in addition to the presence of a *n*-LC phase, may be important in the kinetics of uniaxial chain alignment.

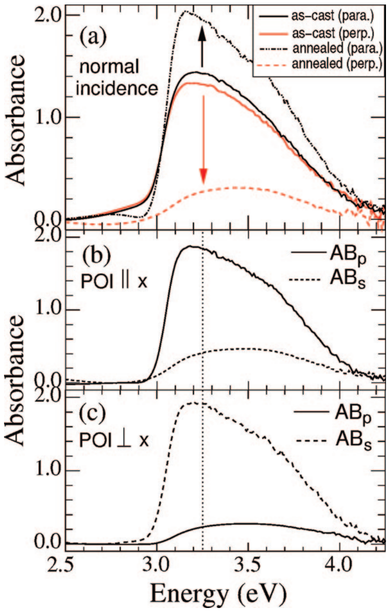

Figure 4. Polarized UV−vis absorption of a PF2/6 film cast from a 5% PF2/6−toluene solution (nominally 150 nm thick) with (a) normal incidence light with the absorption before and after thermal annealing, (b) oblique incidence with the plane of incidence parallel to the rubbing direction, and (c) oblique incidence with the plane of incidence perpendicular to the rubbing direction.

Table 2. Comparison of Structural Order Parameters from a ca. 150 nm Thick PF2/6 Film (Cast from 5% Solution) Using Optical Absorption Data Recorded with an Oblique 45° Angle of Incidence (See Experimental Section for Details)

calculated					
N_x	N_y	N_z	DR	$AB_{s\perp}/AB_{p\parallel}$	$AB_{s\parallel}/AB_{p\perp}$
0.865	0.135	0	6.4	1.3	1.5
0.76	0.12	0.12	6.4	1.25	1.0
0.64	0.10	0.26	6.4	1.1	1.6
experimental			6.3	1.03	1.6

Although the report of Pattison et al.[34] employed a related fluorene−thiophene copolymer, it is interesting to note that this copolymer first exhibited enhanced uniaxial alignment at temperatures below the temperature at which the bulk underwent a crystal to nematic LC phase transition. The PF2/6 UV−vis data assess bulk. If this surface behavior is common to PF2/6, then the reduction in the onset temperature in the thinner PF2/6 films may indicate that the ordering process initiates near or at the top surface.

NEXAFS. NEXAFS provides details regarding the chain orientation at the PF2/6 top surface if the relationship between the TDMs and the polymer chain axis is known. As already noted, the TDM of the 1s to π^* transition (at 285.45 eV) is nearly perpendicular to the chain axis. We also mention that the surface roughness of LMW-PF2/6, as measured by X-ray reflectivity, is very low (ca. 3 nm for film thicknesses up to 180 nm). The AFM image of Figure 2a is consistent with this assertion. Therefore, the NEXAFS signal comes primarily from a smooth surface and not from islands or sharp ridges.[52] Representative total electron yield (TEY) spectra, post-thermal annealing from the medium 30 nm thick film, are shown in Figure 5. Additional spectra are included in the Supporting Information. Systematic changes in the intensity of the 1s to π^* transition peak in the parallel configuration scans ($\varphi = 90°$) with polar angle θ are indicative of increased chain alignment parallel to the rubbing direction. TEY spectra at $\theta = 90°$, 75°, 60°, 45°, and 30° are shown, and the C 1s to π^* resonance peak increases with decreasing polar angle. In PF2/6 this resonance reflects the conjugated character of the aromatic biphenyl rings. For the annealed sample shown in Figure 5 the TEY intensity is lowest at $\theta = 90°$ because the electric field vectors of incident X-rays are parallel to the PF2/6 chain axis direction whereas the TDM of the transition are cylindrically arranged and nearly orthogonal to this axis in the perpendicular configuration. In the perpendicular scans this 285.45 eV resonance peak is large and nearly independent of polar angle.

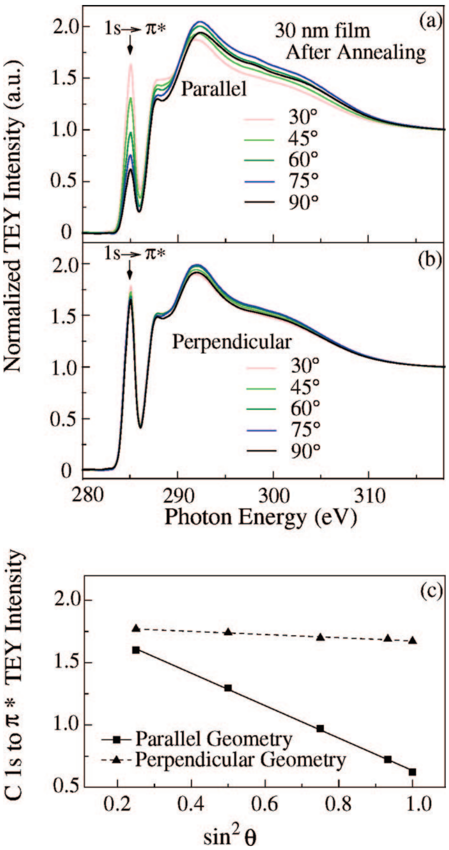

Figure 5. Example NEXAFS data from an aligned PF2/6 film (ca. 30 nm thick) spin-cast on rubbed PI after annealing. "Parallel geometry" refers to *E*-field parallel to the rubbing direction ($\varphi = 0°$ in Figure 1). The polarization dependence is much stronger for the electric field parallel to the rubbing direction (top), indicating alignment of the polymer chains at the surface.

For a more quantitative assessment we employ the same procedure as Pattison et al.[34] by plotting the 1s to π^* resonance peak intensity versus $\sin^2 \theta$ (see the Experimental Section) under the assumption that the templating substrate tilt angle angle, γ, is zero. This method employs a formalism originally forwarded by Stöhr and co-workers.[49,50] The order parameter, S, varies from 0 to 1 as the magnitude of chain alignment parallel to the x-axis increases. The three TDM orientation parameters exhibit similar trends with f_x decreasing, f_y increasing and f_z remaining relatively constant (see Table 3). The observed values are comparable those reported in the fluorene−thiophene polymer in the study by Pattison et al.[34]

The three orientational order coefficients (N_x, N_y, and N_z), included in Table 1, demonstrate that all three series I as-cast films have moderate levels of homogeneous alignment at the top surface (i.e., $N_z < 0.33$). For both the 15 and 30 nm thick samples there is measurable chain alignment parallel to the rubbing direction (i.e., $N_x > N_y$) prior to thermal annealing. Most NEXAFS orientational order parameters are typically less than their respective UV−vis counterpart. With increasing film thickness one would expect poorer chain alignment at the top surface as it resides further away from the templating substrate.

Table 3. Resulting TDM Orientation Parameters for the *x*, *y*, and *z* Directions and the Order Parameter, $S \equiv 1 - 3f_x$, Using the Methodology of Stöhr et al[50] and Pattison et al.[34]

	f_x	f_y	f_z	S^a
series I				
as-cast (15 nm)	0.240 ± 0.007	0.348 ± 0.007	0.402 ± 0.007	0.28 ± 0.02
annealed	0.117 ± 0.003	0.421 ± 0.004	0.455 ± 0.004	0.65 ± 0.01
as-cast (30 nm)	0.260 ± 0.016	0.284 ± 0.013	0.454 ± 0.015	0.22 ± 0.05
annealed	0.118 ± 0.005	0.427 ± 0.005	0.449 ± 0.005	0.65 ± 0.02
as-cast (60 nm)	0.276 ± 0.014	0.279 ± 0.013	0.444 ± 0.013	0.17 ± 0.04
annealed	0.115 ± 0.009	0.429 ± 0.010	0.448 ± 0.010	0.66 ± 0.03
series II				
annealed (15 nm)	0.08 ± 0.04	0.42 ± 0.04	0.48 ± 0.04	0.8
annealed (30 nm)	0.09 ± 0.04	0.49 ± 0.04	0.41 ± 0.04	0.7
annealed (60 nm)	0.08 ± 0.04	0.45 ± 0.04	0.45 ± 0.04	0.8

[a] *S* describes the average orientation of the molecular axes with respect to the rubbing direction.

The anomalously large NEXAFS S_{2D} value in the 15 nm as-cast film is most likely the result of having chains or chain segments that are not perfectly parallel to the surface. The nominal "fraction" of chains or chain segments normal to the surface is typically close to 0.1,[53] and this value is notably less than the 0.26 from the UV−vis absorption analysis for the 150 nm thick film discussed in the preceding section.

After thermal annealing, all specified order parameters (*S*, S_{2D}, S_{3D}) and N_x increase while N_y diminishes.[54] Thermal annealing increases the extent of surface chain alignment parallel to the rubbing direction, and with respect to the assessed N_z uncertainty (of ±0.03), there is no consistent drop in the N_z parameter. In two cases, that of the 30 and 60 nm thick films, any increase in the alignment parallel to the rubbing direction at the film surface occurs without significant changes in the homogeneous (i.e., planar) alignment of the polymer chains. It should be noted that if there is considerable homogeneous surface alignment in the as-cast films, then there there is little if any opportunity for improvement upon annealing.

Most interesting is that comparatively high levels of surface alignment, with $N_x \approx 0.8$, are achieved in all six thermally cycled films studied even though the bulk level of alignment parallel to the rubbing direction drops significantly in the 60 nm thick samples (e.g., a UV−vis DR of just 8.9 is observed in the series I data). For the series I 15 and 30 nm thick samples the extent of surface alignment is somewhat less than that of the bulk, but in the thicker 60 nm film, they are comparable. The negative N_y values in the series II data sets are clearly unphysical. Although the assumption of perfect homogeneous alignment is in itself not physical, the mostly likely origin in this case is from systematic artifacts in this data set.

This analysis also specifies the maximum allowable TDM component parallel to the chain axis, f_c in Table 1, at a value of ∼0.05. The angular tilt relative to the chain axis is 6° [i.e., $\tan^{-1}(0.05/0.475)$], which is close to the value quoted by Bradley and co-workers.[10,41] However, if so, then this would imply that the surface alignment is better than that of the bulk after thermal annealing. In summary, these data, in conjunction with the polarized absorption data, support a thin film structure marked by a graded morphology in which the top and bottom surfaces exhibit a more planar, uniaxial alignment while the film interior contains a greater proportion of tilted (i.e., nonplanar) chains.

Other notable NEXAFS features can be seen at 287.9 and 293.4 eV. The lower energy peak is associated with transitions from the 1s to σ* orbitals of C−H bonds. The broad structure located around 293.4 eV belongs to transitions of 1s to σ* character by C−C bonds. In this case TDM is largest when the electric field vector is parallel to the C−C σ bonds. In PF2/6 we expect this absorption feature to be weakly θ dependent in the parallel configuration and, in contrast to the 1s to π* transition, strongest when the incident X-ray electric field is nearly parallel to the chain axis. As can be seen in Figure 5a, the 1s to σ* transition is typically strongest at $\pi/2 - \theta = 75°$, a value qualitatively consistent with this description. Obtaining a more quantitative measure of the orientation function from this peak is not as straightforward as in the case of the 1s to π* transition because of the wider distribution of the transition dipoles for the σ* orbitals (see Figure 1c) and the increased background in the NEXAFS data.

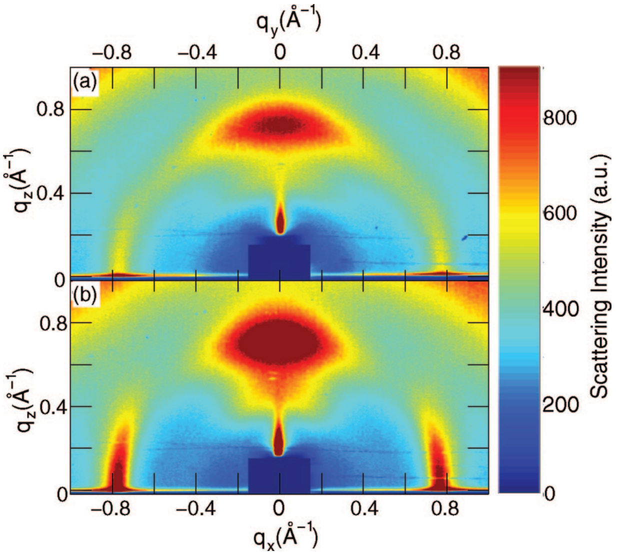

Figure 6. 2D GIXRD patterns of low-molecular-weight PF2/6 polymer ca. 30 nm thick film (spin-cast from 1% solution) on top of a rubbed polyimide substrate before thermal annealing with incident X-ray beam (a) nearly parallel to the *x*-axis and (b) nearly parallel to the *y*-axis.

Grazing-Incidence X-ray Diffraction. GIXRD has a typical penetration depth that ranges between 10 and 100 nm, and therefore these data reflect the average structure across most if not all of the PF2/6 film. Figure 6 plots 2D GIXRD patterns of a typical as-cast PF2/6 film prepared from a 1.0% solution (ca. 30 nm thick). The top image, taken with the incident X-ray beam parallel to the *x*-axis (see Figure 1), is identified with the $q_y - q_z$ scattering plane, and this scattering, characteristic of a nematic glass, has a very strong angular anisotropy with a broad but distinctive $q = 0.75$ Å^{-1} peak and a weaker shoulder near 0.42 Å^{-1}. These features are clearly most intense along the out-of-plane direction (i.e., along q_y with $q_x = 0$). In plane (along q_x with $q_y = 0$) there is evidence of a sharper peak centered at $q = 0.78$ Å^{-1}, and this reflects the fluorene monomer periodicity along the chain axis.[30,32] This latter feature is consistent with a measurable fraction of the nematic domains preferrentially oriented perpendicular to the rubbing direction. The bottom image, Figure 6b, images the $q_x - q_z$ scattering plane. Here the $q = 0.75$ Å^{-1} peak is even more strongly identified along the q_z-axis. The in-plane $q = 0.78$ Å^{-1} meridional peak is noticeably more intense and arcs upward in direct correspondence to domains having out-of-plane mosaic tilts. In summary, these data are consistent with partial planar alignment of the frozen nematic domains but with an extensive cylindrical mosaic about the q_z-axis.

Figure 7 displays 2D patterns of 15, 30, and 60 nm films cast respectively from 0.5%, 1.0%, and 2.0% solutions after thermal annealing. At this low MW these PF2/6 GIXRD patterns exhibit only a few broad scattering peaks originating from frozen nematic domains, rather than the many sharp (*hk*0) reflections[55] characteristic of the hexagonal phase. In the top three scans, labeled (a), (c), and (e), the incident X-ray beam is again nearly parallel to the *x*-axis, and now, because of greater uniaxial alignment, these data approximate the equatorial "(*hk*0)" scat-

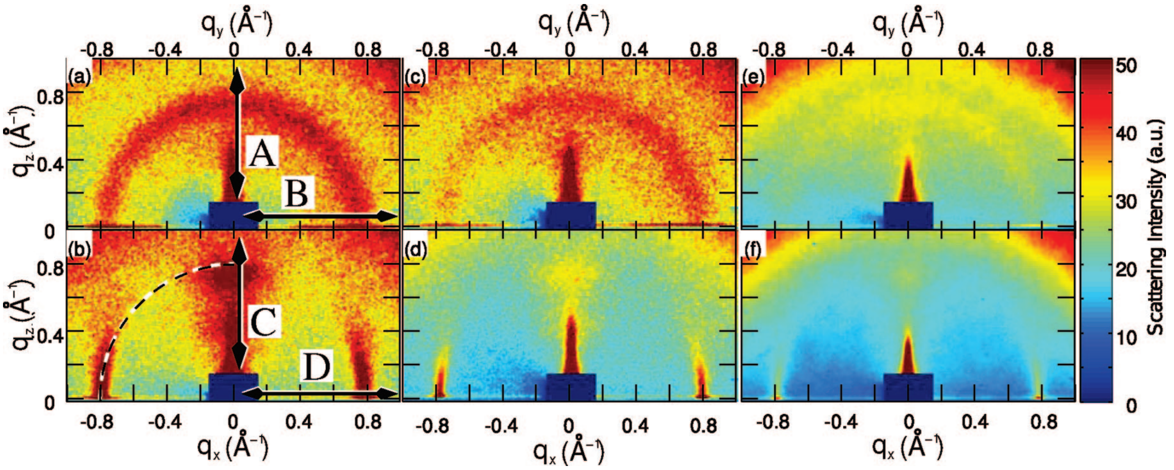

Figure 7. 2D GIXRD patterns of low-molecular-weight PF2/6 polymer thin films spin-cast on top of a rubbed polyimide substrate after thermal annealing. The three top 2D maps, (a), (c), and (e), are from the 60, 30, and 15 nm thick films, respectively, and here the incident X-rays were directed along the rubbing direction. These maps reflect scattering from or near the equatorial (*hk*0) plane (or $y-z$ in regard to Figure 1). At the bottom, (b), (d), and (f) are scattering patterns from the same films, but in this case the incident X-rays are directed perpendicular to the rubbing direction and thus depict scattering from (*h*0*l*) planes (or $x-z$ in regards to Figure 1). Arrows labeled A and C identify the out-of-plane direction, whereas B and D identify the in-plane direction.

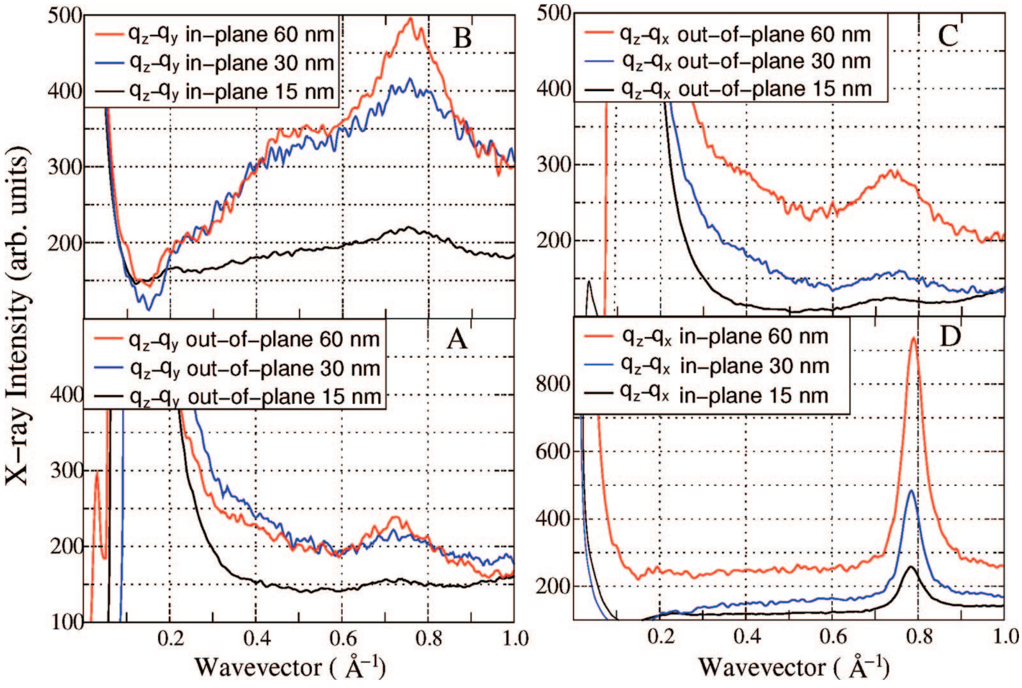

Figure 8. One-dimensional scattering intensities along the directions as indicated by the arrows labeled A–D in Figure 5. A, B, and C reflect scattering intensities approximating the equatorial plane, whereas D is dominated by meridional scattering.

tering plane. The bottom three images, with the X-ray beam nearly parallel to the *y*-axis, now include scattering data from the equatorial to meridional [i.e., from (*h*0*l*) to (0*kl*)] planes. The intensity of the scattering patterns is in rough proportion to the film thickness.[56]

Despite the high optical absorption DRs experimentally measured, the meridional $q = 0.78$ peak still retains appreciable out-of-plane arcing arising from mosaic tilts. In addition, there is some layer-line streaking suggestive of interchain axial disorder. The equatorial scattering is still dominated by the peak centered at $q = 0.75$ Å^{-1} broad and the weak shoulder at $q = 0.42$ Å^{-1}, but accompanying the development of chain alignment parallel to the rubbing direction, this scattering has become more uniformly distributed within the q_y-q_z plane.

These features are more prominent in the thicker films, and additionally, there is evidence for structural anisotropy about the equatorial plane. Figure 8 displays the one-dimensional scattering intensities along the respective directions as indicated by the arrows labeled A–D in Figure 7. A, B, and C reflect scattering intensities approximating the equatorial plane, whereas D is dominated by meridional scattering. The line shape of the meridional peak at $q = 0.78$ Å^{-1} is independent of thickness but, with increasing film thickness, shifts 0.5% to higher wave vector. The scattering at $q = 0.42$ Å^{-1} is most apparent in Figure 8B. The scattering vector here is in-plane. This peak is masked by the strong, specular scattering in the out-of-plane data sets (i.e., A and C) but can be discerned in the 2D GIXRD spectra of Figure 7. The relative intensity of the $q = 0.75$ Å^{-1} peak increases roughly a factor of 2 in comparison with in- and out-of-plane spectra, whereas the $q = 0.42$ Å^{-1} feature, after accounting for the specular scattering background, increases by a somewhat larger factor. This indicates a variation in the

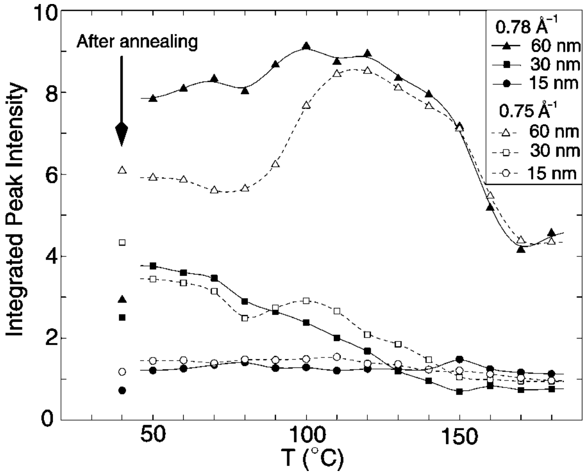

Figure 9. Integrated 1D meridional, $q = 0.78$ Å^{-1}, and equatorial, $q = 0.75$ Å^{-1} (along C, Figure 7), peak intensities during thermal annealing from PF2/6 films spin-cast from 0.5% (15 nm), 1.0% (30 nm), and 2.0% (60 nm) solutions.

equatorial structure parallel and perpendicular to the film surface. This may occur in either amorphous or nematic regions of the film.

Also interesting are the changes in the integrated 1D meridional, $q = 0.78$ Å^{-1}, and equatorial, $q = 0.75$ Å^{-1} (along C, Figure 7), peak intensities during thermal annealing as shown in Figure 9. Both peaks show little variation with temperature in the 15 nm film (i.e., cast from a 0.5% solution). In the 30 nm thickness film (i.e., 1%) there is a slight increase in the equatorial scattering peak starting at 80 °C. This attribute is quite pronounced in the 60 nm film (2%). The onset temperature of the rise closely matches the reported glass transition temperature, and this increased intensity likely originates from the process of "cold crystallization" and improved ordering within nematic domains. This occurs prior to any major changes in the chain orientation of the bulk and, in view of the 15 nm thick film results, is likely suppressed at the film interface. At higher temperatures, 110 °C and above, scattering peak drops in intensity. Two factors likely contribute to this effect: first is the drop due to thermal motion, and second is the occurrence of a broad transition from the nematic phase to an isotropic melt. Once again these attributes are not readily apparent in the thinnest film. Upon returning to rt the intensity remains well below that of the starting point.

The meridional, $q = 0.78$ Å^{-1}, integrated peak intensity exhibits a monotonic decrease with temperature in the 30 nm film, whereas it slightly increases and then rapidly drops at temperatures above 120 °C in the thickest film. The intensity does recover somewhat on cooling back to room temperature but clearly does not track the progression to high optical dichroic ratios or the increase in the surface chain alignment.

All of these GI XRD patterns image a relatively narrow slice of the reciprocal lattice and, even at $q = 0.8$ Å^{-1}, there is only a 4° offset from the meridional and equatorial planes (resulting from the geometry of the Ewald sphere). Thus, these integrated intensities are very specific to domains having homogeneous, uniaxial alignment. The absence of any significant increase in the meridional 0.78 Å^{-1} peak is especially telling in this respect. All told, these data are consistent with a model of structural evolution in which a significant proportion of PF2/6 chains within nematic domains become more parallel to the rubbing direction without increasing the extent of planar alignment. Thermal annealing at temperatures well above the *n*-LC transition temperature may generally increase the net alignment parallel to the rubbing direction, but these X-ray results indicate that the number of chains (or chain segments) having "perfect" homogeneous, uniaxial alignment and/or enhanced ordering within a nematic domain is reduced.

Discussion and Conclusions

The uniaxial chain alignment of low-molecular-weight PF2/6 thin films cast atop rubbed polyimide templates has been characterized, and each of the three methods used in this study provides complementary information. Taken together, there are a number of consistent observations. At room temperature the as-cast films appear in a glassy nematic state with considerable planar alignment both in the interior and at the top surface. With increasing film thickness these as-cast films exhibit some expected properties; film thicknesses in excess of 30 nm are associated with a general reduction in the surface and bulk chain alignment parallel to the rubbing direction.

At temperatures near 100 °C this PF2/6 undergoes a thermotropic transition from the frozen nematic glass to a nematic liquid crystal state. The onset PF2/6 chain reorientation in these films typically occurs at temperatures 20−30 °C above the nominal bulk thermotropic liquid crystal transition temperature. After thermal cycling to temperatures above 220 °C the thin surface layer achieves roughly the same level of chain alignment parallel to the rubbing direction in all cases despite the overall drop in the bulk DR in thicker films. It may be possible that the surface interface acts to maintain or amplify the orientation of the PF2/6 chains so that an optimal level of surface chain alignment is achieved. The origin of this behavior could be microscopic and reflect a molecular level influence of the nematic alignment between near-neighbor chains. Alternatively, there may be a more macroscopic process,[57] such as dewetting[58] and/or anisotropic stress and strain, that results from the textured substrate and subsequent rapid drying of the film.[59] The current study cannot resolve the underlying causes.

GIXRD data verify the presence of a nematic domain structure which undergoes transformation to a more aligned state without an increase in the overall homogeneous alignment of the nematic domains. Thermal annealing at temperatures well above the *n*-LC transition temperature may generally increase the net alignment parallel to the rubbing direction, but these X-ray results indicate that the number of chains (or chain segments) having an "ideal" homogeneous, uniaxial alignment and/or the perfection within a nematic domain is reduced.

All told these data support a structural model in which there is a graded morphology such that the top and bottom surfaces exhibit planar, uniaxial alignment while the film interior is generally less well ordered and includes both planar and nonplanar chains. The highest overall level of bulk uniaxial alignment is obtained in films under 30 nm thick. We expect that these morphological properties can strongly affect organic electronic device properties.

Acknowledgment. The NSF (DMR-0350383, M.J.W.; DMR-0520527, X.L.) and Research Corporation (H.C.) grant support are gratefully acknowledged. The GIXRD portion of this work was supported by an EC grant (RII3-CT-2004-506008 (IA-SFS)). NEXAFS work was performed at the Advanced Light Source which is supported by the Office of Science, Office of Basic Energy Sciences, U.S. Department of Energy, under Contract DE-AC03-76SF00098 and at the Wisconsin Synchrotron Radiation Center which is supported by the National Science Foundation under DMR-0537588. We thank K. T. Hartwig and W. Caliebe for assistance. M.J.W. thanks David Huber, Andy Monkman, and Frank Weinhold for many insightful discussions.

Supporting Information Available: Plots of the full set of NEXAFS data from the "series I" run. This material is available free of charge via the Internet at http://pubs.acs.org.

References and Notes

(1) Forrest, S. R. *Nature (London)* **2004**, *428*, 918.
(2) Cornil, J.; Beljonne, D.; Calbert, J. P.; Brédas, J. L. *Adv. Mater.* **2001**, *13*, 1053.
(3) Samuel, I. D. W. *Philos. Trans. R. Soc. London A* **2000**, *358*, 193.
(4) Forrest, S.; Burrows, P.; Thompson, M. *IEEE Spectrum* **2000**, *37*, 29.
(5) Scherf, U.; List, E. J. W. *Adv. Mater.* **2002**, *14*, 477.
(6) Kawana, S.; Durrell, M.; Lu, J.; Macdonald, J. E.; Grell, M.; Bradley, D. D. C.; Jukes, P. C.; Jones, R. A. L.; Bennett, S. L. *Polymer* **2002**, *43*, 1907.
(7) Sirringhaus, H.; Wilson, R. J.; Friend, R. H.; Inbasekaran, M.; Wu, W.; Woo, E. P.; Grell, M.; Bradley, D. D. C. *Appl. Phys. Lett.* **2000**, *77*, 406.
(8) Ramsdale, C. M.; Greenham, N. C. *J. Phys. D: Appl. Phys.* **2003**, *36*, L29.
(9) Lyons, B. P.; Monkman, A. P. *J. Appl. Phys.* **2004**, *96*, 4735.
(10) Grell, M.; Bradley, D. D. C. *Adv. Mater.* **1999**, *11*, 895.
(11) Voss, K. F.; Foster, C. M.; Smilowitz, L.; Mihailovic, D.; Askari, S.; Srdanov, G.; Ni, Z.; Shi, S.; Heeger, A. J.; Wudl, F. *Phys. Rev. B* **1991**, *43*, 5109.
(12) Tanigaki, N. *Kobunshi Ronbunshu* **2000**, *57*, 515.
(13) Nagamatsu, S.; Takashima, W.; Kaneto, K.; Yoshida, Y.; Tanigaki, N.; Yase, K.; Omote, K. *Macromolecules* **2003**, *36*, 5252.
(14) Jung, Y.; Cho, T. Y.; Yoon, D. Y.; Frank, C. W.; Luning, J. *Macromolecules* **2005**, *38*, 867.
(15) Brinkmann, M. *Macromolecules* **2007**, *40*, 7532.
(16) Wittman, J. C.; Smith, P. *Nature (London)* **1992**, *352*, 414.
(17) Misaki, M.; Ueda, Y.; Nagamatsu, S.; Yoshida, Y.; Tanigaki, N.; Yase, K. *Macromolecules* **2004**, *37*, 6926.
(18) Misaki, M.; Chikamatsu, M.; Tanigaki, N.; Yamashita, M.; Ueda, Y.; Yase, K. *Adv. Mater.* **2005**, *17*, 297.
(19) Paek, S. H.; Durning, C. J.; Lee, K. W.; Lien, A. *J. Appl. Phys.* **1998**, *83*, 1270.
(20) Yao, Y.-H.; Yang, S.-H.; Hsu, C.-S. *Polymer* **2006**, *47*, 8297.
(21) Yang, X. H.; Neher, D.; Lucht, S.; Nothofer, H.; Guntner, R.; Scherf, U.; Hagen, R.; Kostromine, S. *Appl. Phys. Lett.* **2002**, *81*, 2319.
(22) Fukuda, K.; Seki, T.; Ichimura, K. *Macromolecules* **2002**, *35*, 2177.
(23) Matsunaga, D.; Tamaki, T.; Ichimura, K. *J. Mater. Chem.* **2003**, *13*, 1558.
(24) Banach, M. J.; Friend, R. H.; Sirringhaus, H. *Macromolecules* **2003**, *36*, 2838.
(25) Kline, R. J.; McGehee, M. D. *Polym. Rev.* **2006**, *46*, 27.
(26) Neher, D. *Macromol. Rapid Commun.* **2001**, *22*, 1366.
(27) Knaapila, M.; Stepanyan, R.; Torkkeli, M.; Lyons, B. P.; Ikonen, T. P.; Almasy, L.; Foreman, J. P.; Serimaa, R.; Guntner, R.; Scherf, U.; Monkman, A. P. *Phys. Rev. E* **2005**, *71*, 041802.
(28) Knaapila, M.; Stepanyan, R.; Lyons, B. P.; Torkkeli, M.; Hase, T. P. A.; Serimaa, R.; Guntner, R.; Seeck, O. H.; Scherf, U.; Monkman, A. P. *Macromolecules* **2005**, *38*, 2744.
(29) Knaapila, M.; Stepanyan, R.; Lyons, B. P.; Torkkeli, M.; Monkman, A. P. *Adv. Funct. Mater.* **2006**, *16*, 599.
(30) Lieser, G.; Oda, M.; Miteva, T.; Meisel, A.; Nothofer, H. G.; Scherf, U.; Neher, D. *Macromolecules* **2000**, *33*, 4490.
(31) Tanto, B.; Guha, S.; Martin, C. M.; Scherf, U.; Winokur, M. J. *Macromolecules* **2004**, *37*, 9438.
(32) Knaapila, M.; Torkkeli, M.; Monkman, A. P. *Macromolecules* **2007**, *40*, 3610.
(33) Murphy, A. R.; Chang, P. C.; VanDyke, P.; Liu, J. S.; Frechet, J. M. J.; Subramanian, V.; DeLongchamp, D. M.; Sambasivan, S.; Fischer, D. A.; Lin, E. K. *Chem. Mater.* **2005**, *17*, 6033.
(34) Pattison, L. R.; Hexemer, A.; Kramer, E. J.; Petroff, P. M.; Fischer, D. A. *Macromolecules* **2006**, *39*, 2225.
(35) Ho, P. K. H.; Chua, L. L.; Dipankar, M.; Gao, X. Y.; Qi, D. C.; Wee, A. T. S.; Chang, J. F.; Friend, R. H. *Adv. Mater.* **2007**, *19*, 215.
(36) DeLongchamp, D. M.; Kline, R. J.; Lin, E. K.; Fischer, D. A.; Richter, L. J.; Lucas, L. A.; Heeney, M.; McCulloch, I.; Northrup, J. E. *Adv. Mater.* **2007**, *19*, 833.
(37) Gurau, M. C.; Delongchamp, D. M.; Vogel, B. M.; Lin, E. K.; Fischer, D. A.; Sambasivan, S.; Richter, L. J. *Langmuir* **2007**, *23*, 834.
(38) Galambosi, S.; Knaapila, M.; Soininen, J. A.; Nygard, K.; Huotari, S.; Galbrecht, F.; Scherf, U.; Monkman, A. P.; Hamalainen, K. *Macromolecules* **2006**, *39*, 9261.
(39) DeLongchamp, D. M.; Ling, M. M.; Jung, Y.; Fischer, D. A.; Roberts, M. E.; Lin, E. K.; Bao, Z. N. *J. Am. Chem. Soc.* **2006**, *128*, 16579.
(40) Kim, D. H.; Jang, Y.; Park, Y. D.; Cho, K. *Macromolecules* **2006**, *39*, 5843.
(41) Schartel, B.; Wachtendorf, V.; Grell, M.; Bradley, D. D. C.; Hennecke, M. *Phys. Rev. B* **1999**, *60*, 277.
(42) Mosteller, L. P.; Wooten, F. *J. Opt. Soc. Am.* **1968**, *58*, 511.
(43) Wang, H. M. *J. Opt. Soc. Am. A* **1994**, *11*, 2331.
(44) Zharnikov, M.; Frey, S.; Heister, K.; Grunze, M. *J. Electron Spectrosc. Relat. Phenom.* **2002**, *124*, 15.
(45) Samant, M. G.; Stöhr, J.; Brown, H. R.; Russell, T. P.; Sands, J. M.; Kumar, S. K. *Macromolecules* **1996**, *29*, 8334.
(46) Li, L.; Hitchcock, A. P.; Robar, N.; Cornelius, R.; Brash, J. L.; Scholl, A.; Doran, A. *J. Phys. Chem. B* **2006**, *110*, 16763.
(47) Chua, L. L.; Dipankar, M.; Sivaramakrishnan, S.; Gao, X. Y.; Qi, D. C.; Wee, A. T. S.; Ho, P. K. H. *Langmuir* **2006**, *22*, 8587.
(48) Frischand, M. J.; et al. *Gaussian 03, Revision 0.02*; Gaussian, Inc.: Wallingford, CT, 2004.
(49) Stöhr, J.; Samant, M. G. *J. Electron Spectrosc. Relat. Phenom.* **1999**, *99*, 189.
(50) Stöhr, J.; Samant, M. G.; Cossy-Favre, A.; Diaz, J.; Momoi, Y.; Odahara, S.; Nagata, T. *Macromolecules* **1998**, *31*, 1942.
(51) Winokur, M. J.; Cheun, H.; Knaapila, M.; Monkman, A. P.; Scherf, U. *Phys. Rev. B* **2007**, *75*, 113202.
(52) Knaapila, M.; Kisko, K.; Lyons, B. P.; Stepanyan, R.; Foreman, J. P.; Seeck, O. H.; Vainio, U.; Palsson, L. O.; Serimaa, R.; Torkkeli, M.; Monkman, A. P. *J. Phys. Chem. B* **2004**, *108*, 10711.
(53) The uncertainties of the various *N*'s and *S*'s are significantly larger that those of the *f*'s because of error propagation and the various assumptions made.
(54) The series II data taken at the ALS were much more impacted by charging effects, and so the calculated *N*'s have uncertainties of order ±0.1.
(55) Knaapila, M.; Lyons, B. P.; Kisko, K.; Foreman, J. P.; Vainio, U.; Mihaylova, M.; Seeck, O. H.; Pålsson, L. O.; Serimaa, R.; Torkkeli, M.; Monkman, A. P. *J. Phys. Chem. B* **2003**, *107*, 12425.
(56) This is clearly the case in the progression of the bottom three Figure 7 images (after annealing) but not so in the top three. The specific reasons are not well understood, but variations in the equatorial and azimuthal anisotropy upon casting may play a role.
(57) Kumar, S.; Kim, J. H.; Shi, Y. *Phys. Rev. Lett.* **2005**, *94*, 077803.
(58) Chung, J. Y.; Youngblood, J. P.; Stafford, C. M. *Soft Matter* **2007**, *3*, 1163.
(59) Yang, H.; LeFevre, S. W.; Ryu, C. Y.; Bao, Z. *Appl. Phys. Lett.* **2007**, *90*, 172116.

MA702579R